

Learning reaction coordinates *via* cross-entropy minimization: Application to alanine dipeptide

Yusuke Mori,¹ Kei-ichi Okazaki,^{2, a)} Toshifumi Mori,^{2, 3, b)} Kang Kim,^{1, 2, c)} and Nobuyuki Matubayasi^{1, d)}

¹⁾*Division of Chemical Engineering, Department of Materials Engineering Science, Graduate School of Engineering Science, Osaka University, Toyonaka, Osaka 560-8531, Japan*

²⁾*Institute for Molecular Science, Okazaki, Aichi 444-8585, Japan*

³⁾*The Graduate University for Advanced Studies, Okazaki, Aichi 444-8585, Japan*

(Dated: 25 October 2021)

We propose a cross-entropy minimization method for finding the reaction coordinate from a large number of collective variables in complex molecular systems. This method is an extension of the likelihood maximization approach describing the committor function with a sigmoid. By design, the reaction coordinate as a function of various collective variables is optimized such that the distribution of the committor p_B^* values generated from molecular dynamics simulations can be described in a sigmoidal manner. We also introduce the L_2 -norm regularization used in the machine learning field to prevent overfitting when the number of considered collective variables is large. The current method is applied to study the isomerization of alanine dipeptide in vacuum, where 45 dihedral angles are used as candidate variables. The regularization parameter is determined by cross-validation using training and test datasets. It is demonstrated that the optimal reaction coordinate involves important dihedral angles, which are consistent with the previously reported results. Furthermore, the points with $p_B^* \sim 0.5$ clearly indicate a separatrix distinguishing reactant and product states on the potential of mean force using the extracted dihedral angles.

I. INTRODUCTION

Characterizing the free energy landscape of complex molecular systems is important for understanding the underlying mechanism of the dynamical processes such as protein isomerizations.^{1,2} The potential of mean force (PMF) has been utilized to describe the complex landscape as a function of an *a priori* selected small number of collective variables (CVs). Various enhanced simulation techniques, *e.g.*, umbrella sampling³, replica exchange method⁴, and metadynamics⁵, have been developed to obtain PMFs efficiently.

The CV generally denotes a variable as a function of the molecular conformation of the system. Examples are distance and angle variables characterizing molecular structures. Stable states, *i.e.*, reactant and product, are energetically distinguished by the saddle point of the PMF profile. If the saddle point plays a role of the transition state (TS) within the framework of transition state theory, the selected CVs serve as the reaction coordinates (RCs).⁶ It is however non-trivial to find the relevant RCs from a large number of CVs. Most importantly, the position of the saddle point is strongly affected by the choice of CVs. This indicates that it is necessary to rigorously examine whether the obtained PMF profile can predict the TS separating stable states.

The committor analysis is the statistical method to find good RCs from the transition paths sampled by molecular dynamics (MD) simulations.⁷ Let A and B denote the reactant and product states that are divided by the TS, respectively. Here, the “committor” $p_B(\mathbf{x})$ is defined as the probability of

the trajectories that reach the state B prior to the state A starting from a conformation \mathbf{x} with the Maxwell–Boltzmann distributed velocity (typically on the order of 100 trajectories). If this \mathbf{x} is located at the TS, $p_B = 1/2$ because of equal probability reaching A and B. In other words, the TS can be defined as a set of conformations such that $p_B = 1/2$ using a good RC $r(\mathbf{x})$. Practically, the committor distribution $p(p_B)$ obtained from large numbers of initial points near the TS has a sharp peak at $p_B = 1/2$. There have been many applications of the committor distribution test when examining the quality of the chosen coordinate.^{8–26}

In the seminal work by Bolhuis *et al.*, the committor analysis has been applied to the isomerization of alanine dipeptide.¹⁰ For characterizing protein isomerizations, the Ramachandran plot, which is a histogram of backbone dihedral angles ϕ and ψ of amino acids, has conventionally been visualized (see Fig. 1(a) for the definition of ϕ and ψ). In vacuum, two energetically stable states, the β -sheet structure (state A) and the left-handed α -helix structure (state B), are characterized by this plot (see Fig. 1(b) for states A and B). However, Bolhuis *et al.* reported that an additional dihedral angle θ is required to appropriately obtain the proper committor distribution (see also Fig. 1(a) for the definition of θ). That is, the Ramachandran plot using two angles ϕ and ψ can distinguish the two states A and B, but is not capable of predicting the TS properly.

The committor analysis for extracting appropriate RCs has been done *via* a “trial-and-error” approach based on physical intuition. Remarkably, Ma and Dinner have developed the genetic neural network method, which was applied to committor values evaluated for various conformations.¹⁵ It was demonstrated that the optimized CVs for describing the committor distribution showing the peak at $p_B = 1/2$ involve the dihedral angle θ in vacuum. This result is consistent with the previous study by Bolhuis *et al.*¹⁰ The importance of the angle θ has also been discussed by Ren, *et al.*¹⁶

^{a)}Electronic mail: keokazaki@ims.ac.jp

^{b)}Electronic mail: mori@ims.ac.jp

^{c)}Electronic mail: kk@cheng.es.osaka-u.ac.jp

^{d)}Electronic mail: nobuyuki@cheng.es.osaka-u.ac.jp

Overall, developing reliable and efficient methods to identify RCs is still a demanding task in MD simulations.^{27–36} Peters, *et al.*, have recently developed an approach using the likelihood maximization method for finding RCs.³⁷ In their method, the likelihood as a function of the committor value was introduced, and combined with an aimless shooting algorithm, which is a variation of the transition path sampling method.³⁸ The aimless shooting generates a binary outcome with respect to the committor value, *i.e.*, $p_B^* = 0$ or 1, for each trajectory from one shooting point. The committor was modeled as the sigmoid function $p_B(r) = [1 + \tanh(r)]/2$, and the likelihood maximized using those outcomes led to the RC r by optimizing linear combinations of the CVs of sampled shooting points.³⁷ The likelihood maximization method has widely been utilized for finding the good RC in various systems.^{39–55}

In this study, we propose a refined approach for identifying the RC using dataset of the pre-evaluated committor value p_B^* that varies continuously from 0 to 1. This method requires more *a priori* calculations for p_B^* than the binary outcomes. However, the continuous nature of the committor will provide a more accurate statistics for the RC. We illustrate that the likelihood maximization is naturally extended to the cross-entropy minimization. Note that these approaches, corresponding to the Logistic regressions in the machine learning literature, often suffer from overfitting.⁵⁶ To prevent overfitting, we introduce the L_2 -norm regularization to the cross-entropy minimization.

The presented cross-entropy minimization method is applied to study the isomerization of alanine dipeptide in vacuum. We use all dihedral angles of the molecule as candidate CVs and perform the cross-entropy minimization with the committor values p_B^* to search the best RC representing the TS. The regularization parameter is heuristically determined by cross-validation using training and test datasets. Finally, we examine the validity of the optimized coordinate by plotting the committor distributions as a function of characteristic CVs.

The remaining sections of this paper are organized as follows. Section II describes the formalism of the cross-entropy minimization as an generalization of the likelihood maximization. We also introduce the L_2 -norm regularization into the objective function. In Section III, we present the computational details with regard to the generation of the p_B^* data and cross-entropy minimization. In Section IV, the numerical results and discussions are described. Finally, our conclusions are drawn in Section V.

II. THEORY

A. Likelihood maximization and cross-entropy minimization

We start from N snapshots of the system that are sampled from the path connecting the reactants A and product B. We describe each snapshot k by M CVs $q_i(\mathbf{x}_k)$, which are functions of the Cartesian coordinates \mathbf{x}_k . The committor calculated at each point from multiple short simulations is denoted

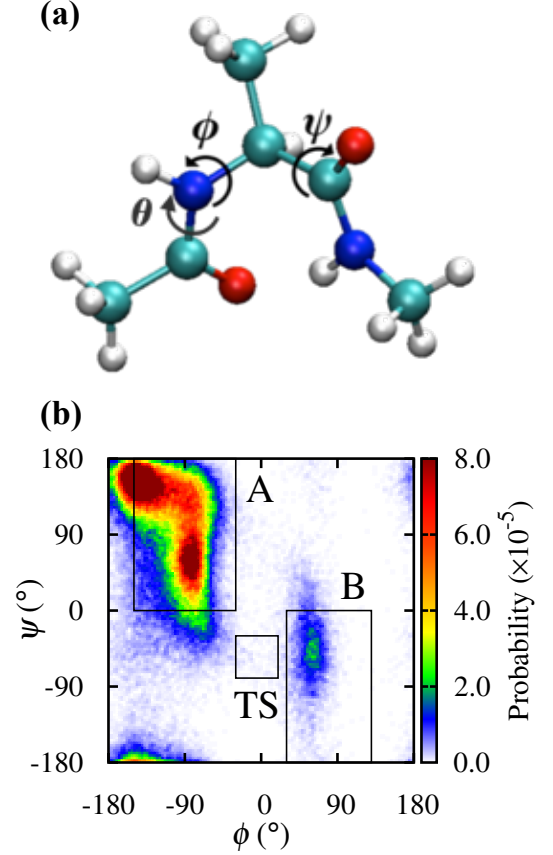


FIG. 1. (a) Schematic representation of the alanine dipeptide molecule and its major dihedral angles, ϕ (C – N – C $_{\alpha}$ – C), ψ (N – C $_{\alpha}$ – C – N), and θ (O – C – N – C $_{\alpha}$). (b) Ramachandran plot of alanine dipeptide in vacuum. The regions described in boxes are defined as A: ($-150^{\circ} \leq \phi \leq -30^{\circ}$, $0^{\circ} \leq \psi \leq 180^{\circ}$), B: ($30^{\circ} \leq \phi \leq 130^{\circ}$, $-180^{\circ} \leq \psi \leq 0^{\circ}$), and TS: ($-30^{\circ} \leq \phi \leq 20^{\circ}$, $-80^{\circ} \leq \psi \leq -30^{\circ}$).

as $p_B^*(\mathbf{x}_k)$.

As discussed by Peters *et al.*, we aim at obtaining a RC that can describe the change of committor distribution p_B^* in a sigmoidal manner. To this end, we define the CV vector $\mathbf{q}(\mathbf{x}_k) = (1, q_1(\mathbf{x}_k), \dots, q_M(\mathbf{x}_k))$ and corresponding coefficients $\alpha = (\alpha_0, \alpha_1, \dots, \alpha_M)$. Note that \mathbf{q} is $(M+1)$ -dimensional due to the bias term ($q_0 = 1$). We describe the trial function $r(\mathbf{q}(\mathbf{x}_k))$ as a linear combination of the CVs as

$$r(\mathbf{q}(\mathbf{x}_k)) = \alpha \cdot \mathbf{q}(\mathbf{x}_k) = \sum_{m=1}^M \alpha_m q_m(\mathbf{x}_k) + \alpha_0. \quad (1)$$

We assume that, in the ideal case, the committor p_B changes from 0 to 1 following the sigmoid function defined by

$$p_B(r(\mathbf{q}(\mathbf{x}_k))) = \frac{1 + \tanh(r(\mathbf{q}(\mathbf{x}_k)))}{2}. \quad (2)$$

Using Eq. (2), the Likelihood function $\mathcal{L}(\alpha)$ can be defined

as

$$\mathcal{L}(\alpha) = \prod_{\mathbf{x}_k \rightarrow B} p_B(r(\mathbf{q}(\mathbf{x}_k))) \times \prod_{\mathbf{x}_k \rightarrow A} (1 - p_B(r(\mathbf{q}(\mathbf{x}_k)))) \quad (3)$$

which was originally introduced by Peters *et al.*³⁷ Here, $\mathbf{x}_k \rightarrow B$ and $\mathbf{x}_k \rightarrow A$ indicate the trajectories starting from point \mathbf{x}_k that ends in state B and A, respectively. By taking the logarithmic form of Eq. (3), we obtain

$$\ln \mathcal{L}(\alpha) = \sum_{\mathbf{x}_k \rightarrow B} \ln p_B(r(\mathbf{q}(\mathbf{x}_k))) + \sum_{\mathbf{x}_k \rightarrow A} \ln [1 - p_B(r(\mathbf{q}(\mathbf{x}_k)))]. \quad (4)$$

While each point \mathbf{x}_k has a fractional probability to reach either state A or B, Eq. (4) can only account for each point in a binary manner to state A ($p_B^*(\mathbf{x}_k) = 0$) or B ($p_B^*(\mathbf{x}_k) = 1$). To make use of the continuous nature of the committor obtained directly, we extend Eq. (4) to

$$\begin{aligned} \mathcal{H}(p_B^*, p_B) \\ = - \sum_{k=1}^N p_B^*(\mathbf{x}_k) \ln p_B(r(\mathbf{q}(\mathbf{x}_k))) \\ - \sum_{k=1}^N (1 - p_B^*(\mathbf{x}_k)) \ln [1 - p_B(r(\mathbf{q}(\mathbf{x}_k)))], \end{aligned} \quad (5)$$

which is equivalent to the cross-entropy. Note that Eq. (5) is derived from the Kullback–Leibler divergence in Ref. 57. Equations (4) and (5) are equivalent with the opposite sign when p_B^* is binary:

$$p_B^* = \begin{cases} 0 & (\mathbf{x}_k \rightarrow A) \\ 1 & (\mathbf{x}_k \rightarrow B) \end{cases} \quad (6)$$

Thus, the likelihood maximization is generalized to the cross-entropy minimization, considering the continuous nature of the committor. Note that $\mathcal{H}(p_B^*, p_B) \geq \mathcal{H}(p_B^*) \equiv \mathcal{H}(p_B^*, p_B = p_B^*)$, where $\mathcal{H}(p_B^*)$ sets the lower bound of the cross-entropy.

B. L_2 -norm regularization

When the number of CVs used to describe the trial function $r(\mathbf{q}(\mathbf{x}_k))$ is large, resulting reaction coordinate *via* the cross-entropy minimization can overfit the input data. To avoid overfitting, we introduced a technique called regularization that considers a penalty term in the objective function. In particular, we used the L_2 -norm regularization.⁵⁶ The objective function with the regularization is,

$$\mathcal{H}(\alpha) = \mathcal{H}(p_B^*, p_B) + \frac{\lambda}{2} \sum_{m=1}^M \alpha_m^2, \quad (7)$$

where λ is the regularization parameter that controls the relative weight of the penalty term. Note that the bias term α_0 is not included in the regularization.

III. COMPUTATIONAL DETAILS

A. Sampling global conformational space

The isomerization of alanine dipeptide in vacuum was studied. One molecule of alanine dipeptide was placed in the 3.16 nm cubic box with the periodic boundary conditions. Time step of 1 fs, neighbor-list distance of 1.5 nm, van der Waals cut-off distance of 1.2 nm, switch function cut-off distance of 1.0 nm were used. For electrostatic interaction, the particle-mesh Ewald method was used with real-space cut-off distance of 1.2 nm. All covalent bonds were constrained by the LINCS algorithm. The AMBER99SB force field was used.⁵⁸ All simulations were conducted with GROMACS2018.1.⁵⁹

The Ramachandran plot was generated from the replica-exchange MD (REMD) simulation.⁴ In the setup of MD simulations, 1 ns equilibration was followed by 10 ns production run with *NVT* condition at 300 K by using the Langevin thermostat. In the REMD simulations, 10 replicas were prepared in the range of 300 - 1209 K with 101 K interval. The exchange ratio and frequency were set to 0.3 and 200 fs, respectively.

B. Sampling conformations in transition state region

As mentioned in Introduction, Peters *et al.*, proposed a variant of transition path sampling called “aimless shooting.”³⁸ In this method, trajectories are generated with freshly sampled momenta from the Maxwell–Boltzmann distribution from every conformation.

In this study, we conducted the two-point version of the aimless shooting following the protocol in Ref. 37. We initiated the aimless shooting from a conformation randomly chosen from the TS region (see below and Fig. 1(b) for the definition of the state). $\tau = 2.01$ ps and $\delta t = 10$ fs were used. Originally, the aimless shooting was introduced to sample conformations near $p_B^* = 1/2$. However, as mentioned in the Introduction, our purpose is to sample points that uniformly cover committor p_B^* values from 0 to 1. For this, we incorporated the shooting point even if the trajectory was rejected. We sampled 2,000 shooting points in total (accepted and rejected trajectories), which are divided equally into training and test datasets. From each point, we quantified p_B^* by running 1 ps MD simulations 100 times with random velocities from the Maxwell–Boltzmann distribution at 300 K.

C. Reaction coordinate optimization *via* cross-entropy minimization

Using the p_B^* values, we performed the cross-entropy minimization. We considered 45 dihedral angles (see Fig. S1 and Table S1 of Supplementary Material). These dihedral angles were transformed into cosine and sine forms, considering the periodicity. Thus, the dimension of α is 91 ($M = 90$ plus 1 bias term). The steepest descent method was used to update

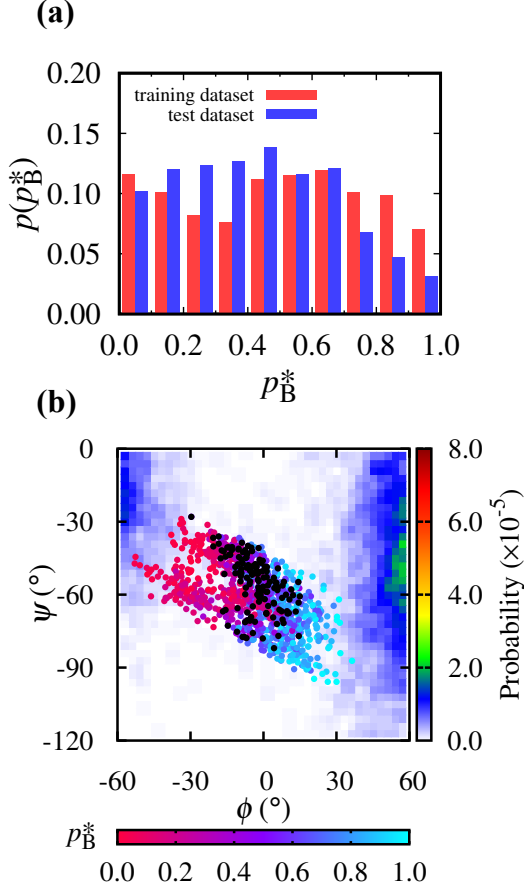


FIG. 2. (a) Probability of committor value p_B^* for the training (red) and test (blue) datasets. Each dataset consists of 1,000 points, and p_B^* for each point is calculated from 100 trajectories. (b) Distribution of the training data points plotted on the Ramachandran plot of Fig. 1(b). The points are colored by the p_B^* values given in the bottom color bar. In addition, the points with $p_B^* \sim 0.5$ ($0.45 \leq p_B^* \leq 0.55$) is marked in black dots.

the coefficients α as,

$$\alpha^{(n+1)} = \alpha^{(n)} - \gamma \nabla \mathcal{H}(\alpha^{(n)}), \quad (8)$$

where $\alpha^{(n)}$ and $\alpha^{(n+1)}$ are the parameters at the n -th and $(n+1)$ -th steps, respectively. $\nabla \mathcal{H}(\alpha^{(n)})$ represents the gradient at the n -th step and γ is the step size which was fixed to 10^{-5} . The optimal α was determined when the norm of $\nabla \mathcal{H}(\alpha)$ becomes less than $\varepsilon = 10^{-3}$. The regularization parameter was chosen as $\lambda = 0, 0.1, 0.5, 1, 10$, and 100 . To check the robustness of the optimization, we ran 10 optimization trials from the initial coefficients α_i that are randomly sampled from the range of $-0.1 \leq \alpha_i \leq 0.1$.

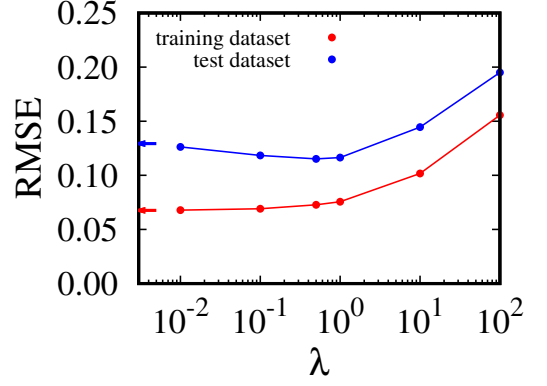


FIG. 3. RMSEs of the training (red) and test (blue) datasets as a function of the regularization parameter λ . RMSE values of $\lambda = 0$ are indicated by the arrows.

TABLE I. First ten dominant coefficients after optimization using $\lambda = 0.5$. The results are given as a mean and standard deviation of 10 trials starting from different initial conditions. The index follows the list given in Table S1 of Supplementary Material.

index	α_i	standard deviation
58	1.7453	2.2132×10^{-3}
55	1.3872	1.4342×10^{-3}
57	-1.2905	1.3520×10^{-3}
12	1.1562	1.2566×10^{-3}
11	-1.0431	1.4347×10^{-3}
30	-0.9451	1.2216×10^{-3}
53	-0.9275	1.2669×10^{-3}
31	0.8127	1.2908×10^{-3}
56	-0.4889	1.1470×10^{-3}
33	-0.4320	1.4202×10^{-3}

IV. RESULTS AND DISCUSSION

A. Training and test datasets of committor values p_B^*

The Ramachandran plot obtained from the REMD trajectory is shown in Fig. 1(b). The two stable states, namely C7_{eq} and C7_{ax}, are found at $\phi \sim -90^\circ$ and $\phi \sim 60^\circ$, respectively. For simplicity, hereafter we denote the C7_{eq} and C7_{ax} states as A and B, respectively. Here we examine paths connecting states A and B, which possibly passes through TS region at $\psi \sim -50^\circ$ and $\phi \sim 0^\circ$. Note that these paths have also been of focus in the previous studies.^{10,15,16} The snapshots along this path are sampled using the aimless shooting protocol as described in Section III B. To optimize and validate the RC, we prepared two datasets, *i.e.*, training and test, each consisting of 1,000 points. The committor value p_B^* for each point was calculated by running 100 short trajectories (see also Section III B). Figure 2(a) shows the committor distribution for the training and test datasets. We see that the two datasets both fully cover $0 \leq p_B^* \leq 1$ with roughly similar probabili-

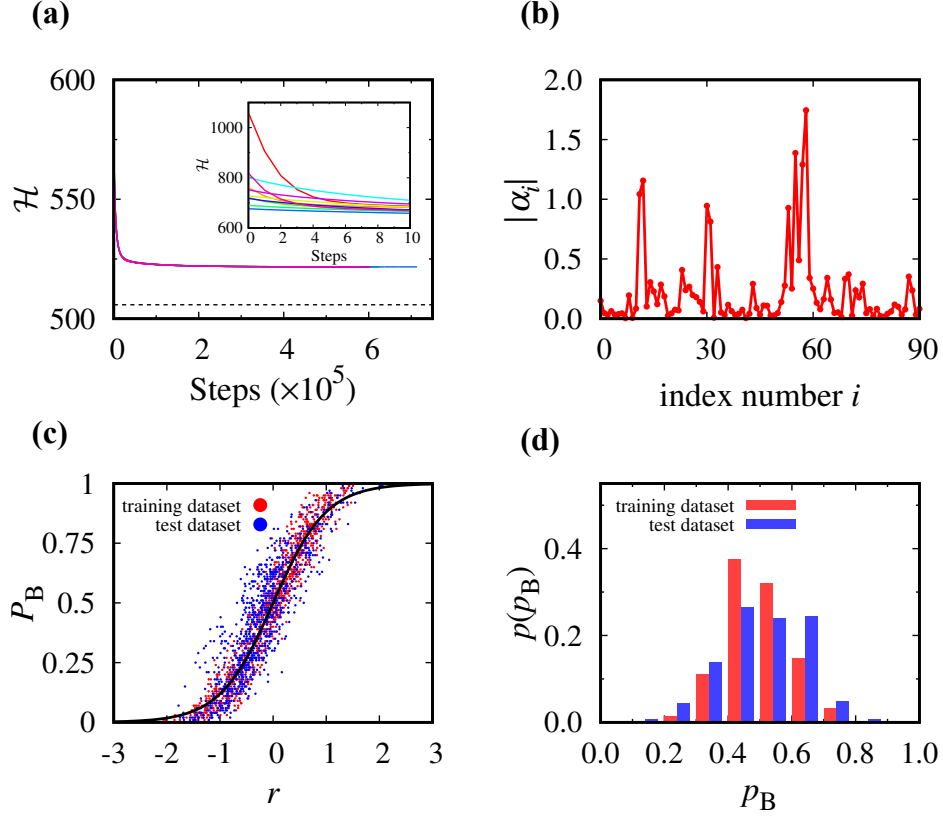


FIG. 4. Summary of the parameter optimization for $\lambda = 0.5$. (a) Changes of the cross-entropy function (\mathcal{H}) during the optimization steps (solid lines) and the ideal value $\mathcal{H}(p_B^*)$ (black dashed line). The results for the 10 trials using different initial α -guesses are shown in different colors. The inset focuses on the first 10 steps, showing that \mathcal{H} differs remarkably in the beginning but quickly converges to a similar value within 10 steps. (b) Optimized coefficients (α_i) in absolute value. Note that the coefficients are determined as an average over the 10 trials. (c) Committor distributions of the training (red) and test (blue) datasets as a function of the optimized coordinate r . The sigmoid function (Eq. (2)) is shown in black line. (d) Probability of p_B at about the TS of r ($-0.2 \leq r \leq 0.2$), where the points are extracted from the data shown in (c).

ties. When the points are plotted on the Ramachandran plot (shown in Fig. 2(b)), we find that ϕ and ψ can roughly separate points reaching state A ($p_B < 1/2$) and B ($p_B > 1/2$). Yet, the points with $p_B^* \sim 0.5$ are spread out in the (ϕ, ψ) space without a clear “separatrix” ($p_B = 1/2$ surface), indicating that the two coordinates are not sufficient in characterizing the TS. This unclear separatrix is in accord with a rather uniform distribution of the committor value p_B^* for the conformations of the TS on the ϕ - ψ plane that was demonstrated *via* the committor analysis in Ref. 10.

B. Minimizing cross-entropy and determining regularization parameter

We optimized the coefficients α that minimize the cross-entropy function $\mathcal{H}(\alpha)$ (Eq. (7)) using the training dataset. To see the effect of the L_2 -norm regularization, we changed the regularization parameter λ in the range of 0 to 100, and performed the parameter optimization and validation. The performance against the training and test datasets were measured by

the root-mean-squared-error (RMSE) between the expected (Eq. (2)) and raw committor values, defined as

$$\text{RMSE}(\lambda) = \sqrt{\frac{1}{N} \sum_{k=1}^N [p_B^*(\mathbf{x}_k) - p_B(r(\mathbf{q}(\mathbf{x}_k)))]^2}, \quad (9)$$

with $N = 1000$ points. The results of RMSEs for different choices of λ are summarized in Fig. 3. The figure shows that as λ is increased, the RMSE of the training data gradually increase; on the contrary, the RMSE of the test data decreases until $\lambda \sim 1$, and starts to increase thereafter. Considering the balance between the performances of the training and test datasets, the optimal choice of λ in the current case was determined to be $\lambda = 0.5$. Below, we focus on the results obtained by fixing λ to 0.5.

C. Validation of the optimized parameter set

We examined the robustness of the optimization procedure using $\lambda = 0.5$. Figure 4(a) shows that the cross-entropy function (\mathcal{H}) consistently converges to the same minimum when

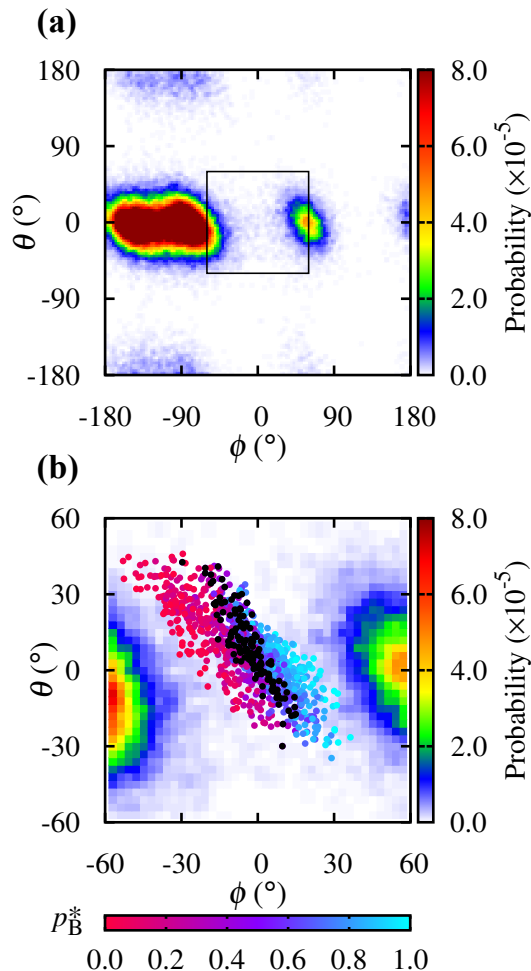


FIG. 5. (a) Contour plot of the probability distribution as a function of ϕ and θ . The probability distribution, calculated from the REMD trajectory, is described by a color bar on the right side of the plot. (b) Distribution of the training data points plotted on the probability distribution given in the squared region of (a). The points are colored by the p_B^* values given in the bottom color bar. In addition, the points with $p_B^* \sim 0.5$ ($0.45 \leq p_B^* \leq 0.55$) is marked in black dots.

the initial guess for α is varied. Figure 4(b) gives the optimized parameters (in absolute number), which is given as a mean of the 10 optimization trials. The result shows that several characteristic coordinates dominate the trial function $r(\mathbf{q}(\mathbf{x}_k))$; the raw number of the major components are summarized in Table I, and its full list is shown in Table S2 of Supplementary Material. For comparison, the results using $\lambda = 0$ and $\lambda = 10$ are also shown in Table S3 and Table S4 of Supplementary Material, respectively.

Using the optimized coefficients, the performance of the predictability is tested using the test dataset. Figure 4(c) compares the distributions of the p_B -value as a function of the optimized coordinate r . We see that overall the training and test datasets follow the sigmoid function (described as a black line in Fig. 4(c)), indicating that the optimized coordinate does serve as a good RC for the two datasets. We note that the

test dataset tends to deviate slightly towards p_B value larger than the sigmoid function. Indeed, this trend can be confirmed by looking at the probability of p_B at about the TS of r ($-0.2 \leq r \leq 0.2$), which is given in Fig. 4(d). The probability show that while the distribution of p_B is sharply peaked at about $p_B \sim 0.5$ for the training dataset, the peak for the test dataset becomes broad and the center is shifted slightly towards $p_B \sim 0.6$. Despite these small differences, the two probabilities can be characterized by a single peak centered at $p_B \sim 0.5$ and with no points at $p_B < 0.1$ and $p_B > 0.9$. The current results thus confirm that the optimal RC determined using the training dataset is able to characterize the TS of the training dataset. Note that the results corresponding to Fig. 4(c) and Fig. 4(d) for $\lambda = 0$ and $\lambda = 10$ are shown in Fig. S2 and Fig. S3 of Supplementary Material, respectively.

D. Character of the optimized reaction coordinate

As described in Fig. 4(b), the optimal coordinate can be characterized with a few dominant CVs. Table I lists the first 10 dominant components found in the optimal coordinate using $\lambda = 0.5$, and the full list is also provided in Table S2 of Supplementary Material. The first two components, α_{58} , and α_{55} , corresponds to the coefficient of $\sin \phi$ (5-7-9-15) and $\sin \theta$ (6-5-7-9), respectively (see also Fig. S1 and Table S1 of Supplementary Material). Note that these coordinates have been proposed to be important by Bolhuis *et al.*¹⁰ The other major components, α_{57} , α_{12} , and α_{11} , are also the rotations about the C – N – C $_{\alpha}$ and C – N bonds (see Fig. 1(a)); ψ only comes as a sixth component (as α_{30}). The rotations about C – N – C $_{\alpha}$ and C – N bonds, which can be characterized by ϕ and θ , respectively, are thus suggested to be critical in characterizing the current TS of interest.

Finally, to confirm this insight, the committor distribution is examined on the probability distribution of ϕ and θ , which was also obtained from the REMD trajectory and plotted in Fig. 5(a). Note that the two states A and B are found at $\phi \sim -90^\circ$ and $\phi \sim 60^\circ$, respectively, whereas the angle θ is mostly located at $\theta \sim 0^\circ$ regardless of the states. The training dataset points are described as a function of ϕ and θ in Fig. 5(b). We see that, in contrast to the ϕ - ψ plot in Fig. 2(b), the points with $p_B^* \sim 0.5$ are narrowly distributed along a diagonal line in the ϕ - θ plot (Fig. 5(b)), indicative of a clearer separatrix. This confirms that coupled changes of ϕ and θ are important for the TS along the path connecting states A and B. It is also consistent with the committor distributions showing the peak at $p_B = 1/2$ evaluated either by the transition state sampling¹⁰ or by the umbrella sampling¹⁵ on the ϕ - θ plane. In conclusion, it is demonstrated the method of the minimization of the cross-entropy function \mathcal{H} combined with the L_2 -norm regularization can guide the straightforward way to find the RC that appropriately describes the TS.

V. CONCLUSIONS

In this paper, we proposed a cross-entropy minimization method to identify the RC from a large number of CVs using the committor dataset p_B^* . The method is a generalization of the likelihood maximization approach proposed by Peters *et al.*,³⁷ and is also derived from the Kullback–Leibler divergence.⁵⁷ To take account of a large number of CVs and yet avoid overfitting, we further introduced the L_2 -norm regularization technique.⁵⁶

Using the training and test datasets of committor p_B^* , which are described as a function of the dihedral angles (in the cosine and sine forms), we minimized the cross-entropy function \mathcal{H} and determined the optimal balance of the regularization penalty. We identified the appropriate RC capable of describing the TS of the isomerization reaction of alanine dipeptide in vacuum. The minimization of \mathcal{H} was found to be quite stable, *i.e.*, the parameters consistently converged to the same set independent of the initial guesses of α . The committor distribution at the TS ($r \sim 0$) was found to be peaked at $p_B \sim 0.5$, both in the cases of the training and data sets. This result indicates that $r = 0$ indeed describes the TS. The optimized coordinate was dominantly characterized by the dihedral angles ϕ and θ . These CVs were further justified by the clear separatrix on the scattering plot on the (ϕ, θ) plane. The presented result is consistent with the observation in the previous studies^{10,15,16}, which showed the importance of θ in characterizing the TS of this reaction.

Finally, it should be emphasized that selecting the appropriate RC becomes often cumbersome when considered CVs are possibly redundant and are also correlated with each other.⁶ The current approach *via* the cross-entropy function combined with the L_2 -norm regularization can be a powerful means to identify and characterize the RC from the p_B^* dataset.

SUPPLEMENTARY MATERIAL

See supplementary material for dihedral angles and CV indices (Fig. S1 and Table S1), full list of optimal coordinate for $\lambda = 0, 0.5$, and 10 (Table S2, Table S3, and Table S4, respectively), committor distributions as a function of the optimized coordinate for $\lambda = 0$ and 10 (Fig. S2), and p_B probability at about the TS of r ($-0.2 \leq r \leq 0.2$) for $\lambda = 0$ and 10 (Fig. S3).

DATA AVAILABILITY STATEMENT

The data supporting the findings of this study are available from the corresponding authors upon reasonable request.

ACKNOWLEDGMENTS

The authors thank Shinji Saito and Takenobu Nakamura for helpful discussions. This work was partially supported by JSPS KAKENHI Grant Numbers: JP18H02415 (K.O.), JP18K05049 (T.M.),

JP18H01188 (K.K.), JP20H05221 (K.K.), and JP19H04206 (N.M.). T.M. and K.K. thank the support from the KAKENHI Innovative Area “Studying the Function of Soft Molecular Systems by the Concerted Use of Theory and Experiment.” K.O. was supported by Building of Consortia for the Development of Human Resources in Science and Technology, MEXT, Japan. This work was also partially supported by the Fugaku Supercomputing Project and the Elements Strategy Initiative for Catalysts and Batteries (No. JPMXP0112101003) from the Ministry of Education, Culture, Sports, Science, and Technology. The numerical calculations were performed at Research Center of Computational Science, Okazaki Research Facilities, National Institutes of Natural Sciences, Japan.

¹C. Chipot and A. Pohorille, *Free Energy Calculations: Theory and Applications in Chemistry and Biology* (Springer, New York, 2007).

²D. M. Zuckerman, *Statistical Physics of Biomolecules: An Introduction* (CRC Press, Boca Raton, 2010).

³G. M. Torrie and J. P. Valleau, “Nonphysical sampling distributions in Monte Carlo free-energy estimation: Umbrella sampling,” *J. Comput. Phys.* **23**, 187–199 (1977).

⁴Y. Sugita and Y. Okamoto, “Replica-exchange molecular dynamics method for protein folding,” *Chem. Phys. Lett.* **314**, 141–151 (1999).

⁵A. Laio and M. Parrinello, “Escaping free-energy minima,” *Proc. Natl. Acad. Sci. U.S.A.* **99**, 12562–12566 (2002).

⁶B. Peters, *Reaction Rate Theory and Rare Events* (Elsevier, Amsterdam, 2017).

⁷P. G. Bolhuis, D. Chandler, C. Dellago, and P. L. Geissler, “Transition path sampling: throwing ropes over rough mountain passes, in the dark,” *Annu. Rev. Phys. Chem.* **53**, 291–318 (2002).

⁸R. Du, V. S. Pande, A. Y. Grosberg, T. Tanaka, and E. S. Shakhnovich, “On the transition coordinate for protein folding,” *J. Chem. Phys.* **108**, 334–350 (1998).

⁹P. L. Geissler, C. Dellago, and D. Chandler, “Kinetic Pathways of Ion Pair Dissociation in Water,” *J. Phys. Chem. B* **103**, 3706–3710 (1999).

¹⁰P. G. Bolhuis, C. Dellago, and D. Chandler, “Reaction coordinates of biomolecular isomerization,” *Proc. Natl. Acad. Sci. U.S.A.* **97**, 5877–5882 (2000).

¹¹C. Dellago, P. G. Bolhuis, and P. L. Geissler, “Transition Path Sampling,” in *Adv. Chem. Phys.*, Vol. 123 (John Wiley & Sons, Ltd, 2002) pp. 1–78.

¹²M. F. Hagan, A. R. Dinner, D. Chandler, and A. K. Chakraborty, “Atomistic understanding of kinetic pathways for single base-pair binding and unbinding in DNA,” *Proc. Natl. Acad. Sci. U.S.A.* **100**, 13922–13927 (2003).

¹³G. Hummer, “From transition paths to transition states and rate coefficients,” *J. Chem. Phys.* **120**, 516–523 (2004).

¹⁴A. C. Pan and D. Chandler, “Dynamics of Nucleation in the Ising Model,” *J. Phys. Chem. B* **108**, 19681–19686 (2004).

¹⁵A. Ma and A. R. Dinner, “Automatic Method for Identifying Reaction Coordinates in Complex Systems,” *J. Phys. Chem. B* **109**, 6769–6779 (2005).

¹⁶W. Ren, E. Vanden-Eijnden, P. Maragakis, and W. E, “Transition pathways in complex systems: Application of the finite-temperature string method to the alanine dipeptide,” *J. Chem. Phys.* **123**, 134109 (2005).

¹⁷Y. M. Rhee and V. S. Pande, “One-Dimensional Reaction Coordinate and the Corresponding Potential of Mean Force from Commitment Probability Distribution,” *J. Phys. Chem. B* **109**, 6780–6786 (2005).

¹⁸W. E, W. Ren, and E. Vanden-Eijnden, “Transition pathways in complex systems: Reaction coordinates, isocommittor surfaces, and transition tubes,” *Chem. Phys. Lett.* **413**, 242–247 (2005).

¹⁹A. Berezhkovskii and A. Szabo, “One-dimensional reaction coordinates for diffusive activated rate processes in many dimensions,” *J. Chem. Phys.* **122**, 014503 (2005).

²⁰R. B. Best and G. Hummer, “Reaction coordinates and rates from transition paths,” *Proc. Natl. Acad. Sci. U.S.A.* **102**, 6732–6737 (2005).

²¹D. Moroni, P. R. ten Wolde, and P. G. Bolhuis, “Interplay between Structure and Size in a Critical Crystal Nucleus,” *Phys. Rev. Lett.* **94**, 343 (2005).

²²B. Peters, “Using the histogram test to quantify reaction coordinate error,” *J. Chem. Phys.* **125** (2006).

- ²³D. Branduardi, F. L. Gervasio, and M. Parrinello, "From A to B in free energy space," *J. Chem. Phys.* **126**, 054103 (2007).
- ²⁴S. L. Quaytman and S. D. Schwartz, "Reaction coordinate of an enzymatic reaction revealed by transition path sampling," *Proc. Natl. Acad. Sci. U.S.A.* **104**, 12253–12258 (2007).
- ²⁵D. Antoniou and S. D. Schwartz, "The stochastic separatrix and the reaction coordinate for complex systems," *J. Chem. Phys.* **130**, 151103 (2009).
- ²⁶B. Peters, "p(TP|q) peak maximization: Necessary but not sufficient for reaction coordinate accuracy," *Chem. Phys. Lett.* **494**, 100–103 (2010).
- ²⁷B. Peters, "Recent advances in transition path sampling: accurate reaction coordinates, likelihood maximisation and diffusive barrier-crossing dynamics," *Mol. Simul.* **36**, 1265–1281 (2010).
- ²⁸W. Li and A. Ma, "Recent developments in methods for identifying reaction coordinates," *Mol. Simul.* **40**, 784–793 (2014).
- ²⁹D. J. Wales, "Perspective: Insight into reaction coordinates and dynamics from the potential energy landscape," *J. Chem. Phys.* **142**, 130901 (2015).
- ³⁰B. Peters, "Reaction Coordinates and Mechanistic Hypothesis Tests," *Annu. Rev. Phys. Chem.* **67**, 669–690 (2016).
- ³¹P. V. Banushkina and S. V. Krivov, "Optimal reaction coordinates," *WIREs Comput Mol Sci* **6**, 748–763 (2016).
- ³²F. Sittel and G. Stock, "Perspective: Identification of collective variables and metastable states of protein dynamics," *J. Chem. Phys.* **149**, 150901 (2018).
- ³³M. M. Sultan and V. S. Pande, "Automated design of collective variables using supervised machine learning," *J. Chem. Phys.* **149**, 094106 (2018).
- ³⁴H. Jung, R. Covino, and G. Hummer, "Artificial Intelligence Assists Discovery of Reaction Coordinates and Mechanisms from Molecular Dynamics Simulations," *arXiv* (2019), 1901.04595v1.
- ³⁵F. Noé, A. Tkatchenko, K.-R. Müller, and C. Clementi, "Machine Learning for Molecular Simulation," *Annu. Rev. Phys. Chem.* (2020).
- ³⁶H. Sidky, W. Chen, and A. L. Ferguson, "Machine learning for collective variable discovery and enhanced sampling in biomolecular simulation," *Mol. Phys.* **17**, 1–21 (2020).
- ³⁷B. Peters, G. T. Beckham, and B. L. Trout, "Extensions to the likelihood maximization approach for finding reaction coordinates," *J. Chem. Phys.* **127**, 034109 (2007).
- ³⁸B. Peters and B. L. Trout, "Obtaining reaction coordinates by likelihood maximization," *J. Chem. Phys.* **125**, 054108 (2006).
- ³⁹G. T. Beckham, B. Peters, C. Starbuck, N. Variankaval, and B. L. Trout, "Surface-Mediated Nucleation in the Solid-State Polymorph Transformation of Terephthalic Acid," *J. Am. Chem. Soc.* **129**, 4714–4723 (2007).
- ⁴⁰G. T. Beckham, B. Peters, and B. L. Trout, "Evidence for a Size Dependent Nucleation Mechanism in Solid State Polymorph Transformations," *J. Phys. Chem. B* **112**, 7460–7466 (2008).
- ⁴¹J. Vreede, J. Juraszek, and P. G. Bolhuis, "Predicting the reaction coordinates of millisecond light-induced conformational changes in photoactive yellow protein," *Proc. Natl. Acad. Sci. U.S.A.* **107**, 2397–2402 (2010).
- ⁴²W. Lechner, J. Rogal, J. Juraszek, B. Ensing, and P. G. Bolhuis, "Nonlinear reaction coordinate analysis in the reweighted path ensemble," *J. Chem. Phys.* **133**, 174110 (2010).
- ⁴³B. Pan and M. S. Ricci, "Molecular Mechanism of Acid-Catalyzed Hydrolysis of Peptide Bonds Using a Model Compound," *J. Phys. Chem. B* **114**, 4389–4399 (2010).
- ⁴⁴G. T. Beckham and B. Peters, "Optimizing Nucleus Size Metrics for Liquid–Solid Nucleation from Transition Paths of Near-Nanosecond Duration," *J. Phys. Chem. Lett.* **2**, 1133–1138 (2011).
- ⁴⁵W. Lechner, C. Dellago, and P. G. Bolhuis, "Role of the Prestructured Surface Cloud in Crystal Nucleation," *Phys. Rev. Lett.* **106**, 085701 (2011).
- ⁴⁶B. Peters, "Inertial likelihood maximization for reaction coordinates with high transmission coefficients," *Chem. Phys. Lett.* **554**, 248–253 (2012).
- ⁴⁷L. Xi, M. Shah, and B. L. Trout, "Hopping of Water in a Glassy Polymer Studied via Transition Path Sampling and Likelihood Maximization," *J. Phys. Chem. B* **117**, 3634–3647 (2013).
- ⁴⁸S. Jungblut, A. Singraber, and C. Dellago, "Optimising reaction coordinates for crystallisation by tuning the crystallinity definition," *Mol. Phys.* **111**, 3527–3533 (2013).
- ⁴⁹R. G. Mullen, J.-E. Shea, and B. Peters, "Transmission Coefficients, Committers, and Solvent Coordinates in Ion-Pair Dissociation," *J. Chem. Theory Comput.* **10**, 659–667 (2014).
- ⁵⁰R. G. Mullen, J.-E. Shea, and B. Peters, "Easy Transition Path Sampling Methods: Flexible-Length Aimless Shooting and Permutation Shooting," *J. Chem. Theory Comput.* **11**, 2421–2428 (2015).
- ⁵¹L. Lupi, B. Peters, and V. Molinero, "Pre-ordering of interfacial water in the pathway of heterogeneous ice nucleation does not lead to a two-step crystallization mechanism," *J. Chem. Phys.* **145**, 211910 (2016).
- ⁵²H. Jung, K.-i. Okazaki, and G. Hummer, "Transition path sampling of rare events by shooting from the top," *J. Chem. Phys.* **147**, 152716 (2017).
- ⁵³M. N. Joswiak, M. F. Doherty, and B. Peters, "Ion dissolution mechanism and kinetics at kink sites on NaCl surfaces," *Proc. Natl. Acad. Sci. U.S.A.* **10**, 201713452 (2018).
- ⁵⁴G. Díaz Leines and J. Rogal, "Maximum Likelihood Analysis of Reaction Coordinates during Solidification in Ni," *J. Phys. Chem. B* **122**, 10934–10942 (2018).
- ⁵⁵K.-i. Okazaki, D. Wöhlert, J. Warnau, H. Jung, Ö. Yildiz, W. Kühlbrandt, and G. Hummer, "Mechanism of the electroneutral sodium/proton antiporter PaNhaP from transition-path shooting," *Nat. Commun.* **10**, 87 (2019).
- ⁵⁶C. Bishop, *Pattern Recognition and Machine Learning* (Springer, New York, 2006).
- ⁵⁷T. Mori and S. Saito, "Dissecting the dynamics during enzyme catalysis: A case study of Pin1 peptidyl-prolyl isomerase," *J. Chem. Theory Comput.* **16**, 3396–4307 (2020).
- ⁵⁸V. Hornak, R. Abel, A. Okur, B. Strockbine, A. Roitberg, and C. Simmerling, "Comparison of multiple Amber force fields and development of improved protein backbone parameters," *Proteins* **65**, 712–725 (2006).
- ⁵⁹M. J. Abraham, T. Murtola, R. Schulz, S. Páll, J. C. Smith, B. Hess, and E. Lindahl, "GROMACS: High performance molecular simulations through multi-level parallelism from laptops to supercomputers," *SoftwareX* **1-2**, 19–25 (2015).

Supplementary Material

Learning reaction coordinates *via* cross-entropy minimization: Application to alanine dipeptide

Yusuke Mori¹, Kei-ichi Okazaki², Toshifumi Mori^{2,3}, Kang Kim^{1,2}, Nobuyuki Matubayasi¹

¹*Division of Chemical Engineering, Graduate School of Engineering Science, Osaka University, Osaka 560-8531, Japan*

²*Institute for Molecular Science, Okazaki, Aichi 444-8585, Japan*

³*The Graduate University for Advanced Studies, Okazaki, Aichi 444-8585, Japan*

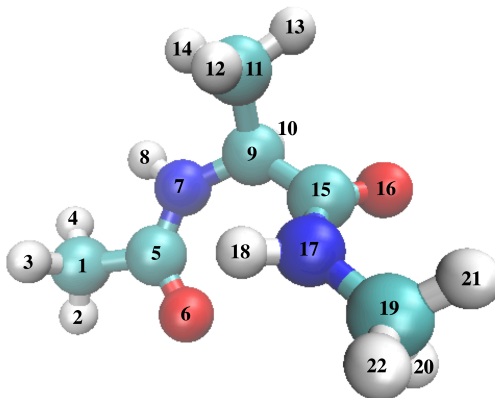


FIG. S1. Schematic representation of the alanine dipeptide molecule and the numbering of atoms.

TABLE S1. Definition of the dihedral angle coordinates corresponding to the coefficients α_i . The atom numbers are defined in Fig. S1. Note that the dihedral angles are used in cosine and sine forms, *i.e.*, α_{01} to α_{45} and α_{46} to α_{90} are the cosine and sine forms, respectively.

index	atom number		
01 – 03	2 - 1 - 5 - 6	2 - 1 - 5 - 7	3 - 1 - 5 - 6
04 – 06	3 - 1 - 5 - 7	4 - 1 - 5 - 6	4 - 1 - 5 - 7
07 – 09	1 - 5 - 7 - 8	1 - 5 - 7 - 9	6 - 5 - 7 - 8
10 – 12	6 - 5 - 7 - 9	5 - 7 - 9 - 10	5 - 7 - 9 - 11
13 – 15	5 - 7 - 9 - 15	8 - 7 - 9 - 10	8 - 7 - 9 - 11
16 – 18	8 - 7 - 9 - 15	7 - 9 - 11 - 12	7 - 9 - 11 - 13
19 – 21	7 - 9 - 11 - 14	10 - 9 - 11 - 12	10 - 9 - 11 - 13
22 – 24	10 - 9 - 11 - 14	15 - 9 - 11 - 12	15 - 9 - 11 - 13
25 – 27	15 - 9 - 11 - 14	7 - 9 - 15 - 16	7 - 9 - 15 - 17
28 – 30	10 - 9 - 15 - 16	10 - 9 - 15 - 17	11 - 9 - 15 - 16
31 – 33	11 - 9 - 15 - 17	9 - 15 - 17 - 18	9 - 15 - 17 - 19
34 – 36	16 - 15 - 17 - 18	16 - 15 - 17 - 19	15 - 17 - 19 - 20
37 – 39	15 - 17 - 19 - 21	15 - 17 - 19 - 22	18 - 17 - 19 - 20
40 – 42	18 - 17 - 19 - 21	18 - 17 - 19 - 22	1 - 7 - 5 - 6
43 – 45	5 - 9 - 7 - 8	9 - 17 - 15 - 16	15 - 19 - 17 - 18

TABLE S2. Full list of optimized coefficients for $\lambda = 0.5$ in descending order. The coefficients are calculated as a mean over 10 optimization trials with different initial parameters, and the standard deviations are also calculated from that data.

index	α_i	standard deviation	index	α_i	standard deviation
58	1.7453	2.2132×10^{-3}	44	0.0893	3.7040×10^{-3}
55	1.3872	1.4342×10^{-3}	10	-0.0852	5.4605×10^{-4}
57	-1.2905	1.3520×10^{-3}	78	0.0831	1.8153×10^{-3}
12	1.1562	1.2566×10^{-3}	90	0.0822	4.9167×10^{-5}
11	-1.0431	1.4347×10^{-3}	76	-0.0797	1.5140×10^{-3}
30	-0.9451	1.2216×10^{-3}	62	-0.0794	1.2742×10^{-3}
53	-0.9275	1.2669×10^{-3}	86	0.0783	4.0652×10^{-4}
31	0.8127	1.2908×10^{-3}	21	0.0752	1.6528×10^{-3}
56	-0.4889	1.1470×10^{-3}	40	0.0751	6.5192×10^{-4}
33	-0.4320	1.4202×10^{-3}	22	-0.0693	1.4945×10^{-3}
23	-0.4079	1.4942×10^{-3}	03	0.0633	1.2441×10^{-3}
70	0.3702	1.8008×10^{-3}	37	0.0629	3.7637×10^{-4}
87	-0.3522	1.1409×10^{-3}	29	-0.0610	1.1698×10^{-3}
64	0.3417	2.4532×10^{-3}	82	-0.0600	7.0894×10^{-4}
59	-0.3412	5.7088×10^{-4}	67	0.0529	1.4246×10^{-3}
69	-0.3336	1.4729×10^{-3}	34	0.0525	9.6742×10^{-4}
14	-0.3058	4.7081×10^{-4}	66	0.0484	1.6093×10^{-3}
74	-0.2931	1.4450×10^{-3}	01	-0.0474	1.2315×10^{-3}
43	-0.2916	3.6195×10^{-4}	50	0.0474	1.3886×10^{-3}
17	-0.2855	2.0916×10^{-3}	75	-0.0458	1.9937×10^{-3}
52	-0.2774	1.8192×10^{-3}	06	0.0448	1.1690×10^{-3}
25	0.2683	1.7937×10^{-3}	20	-0.0446	1.0052×10^{-3}
54	-0.2524	1.8326×10^{-3}	42	-0.0419	2.8231×10^{-3}
60	-0.2518	1.3573×10^{-3}	39	-0.0419	3.9380×10^{-4}
24	0.2390	1.5487×10^{-3}	81	0.0413	8.6112×10^{-4}
72	0.2374	2.9760×10^{-3}	05	-0.0380	1.1829×10^{-3}
88	-0.2369	1.5089×10^{-3}	04	-0.0343	1.2638×10^{-3}
15	-0.2283	1.1347×10^{-3}	89	-0.0342	1.5882×10^{-3}
26	-0.1978	2.2601×10^{-3}	02	-0.0336	1.2283×10^{-3}
08	0.1955	1.1138×10^{-3}	45	-0.0329	1.5147×10^{-4}
18	0.1869	1.4237×10^{-3}	85	0.0328	4.5792×10^{-4}
27	0.1803	2.5249×10^{-3}	38	0.0318	6.1766×10^{-4}
73	0.1789	1.5840×10^{-3}	35	0.0302	2.1288×10^{-3}
63	-0.1638	1.4197×10^{-3}	49	-0.0281	1.2168×10^{-3}
65	-0.1600	1.5497×10^{-3}	71	0.0266	1.6182×10^{-3}
00	-0.1501	1.7866×10^{-2}	48	-0.0265	1.2725×10^{-3}
28	0.1406	1.8230×10^{-3}	19	-0.0254	1.2048×10^{-3}
51	0.1394	1.4095×10^{-3}	79	0.0222	1.7288×10^{-3}
61	-0.1337	1.5507×10^{-3}	77	-0.0218	1.6835×10^{-3}
16	0.1215	3.9594×10^{-4}	80	-0.0165	1.8729×10^{-3}
83	0.1181	3.5624×10^{-4}	68	0.0147	1.3306×10^{-3}
36	0.1160	6.7586×10^{-4}	32	0.0083	1.1014×10^{-3}
46	0.1109	8.6875×10^{-4}	09	0.0060	2.2018×10^{-4}
47	-0.1089	8.5633×10^{-4}	41	-0.0049	5.2831×10^{-4}
13	-0.1017	1.3712×10^{-3}	07	-0.0049	2.2382×10^{-4}
84	0.1005	1.0053×10^{-3}			

TABLE S3. Full list of optimized coefficients for $\lambda = 0$ in descending order. The coefficients are calculated as a mean over 10 optimization trials with different initial parameters, and the standard deviations are also calculated from that data.

index	α_i	standard deviation	index	α_i	standard deviation
58	3.1511	5.1786×10^{-3}	61	0.4045	2.5976×10^{-3}
55	2.6830	1.4032×10^{-2}	78	-0.4023	3.4432×10^{-2}
33	-2.5446	4.1285×10^{-3}	83	0.3947	4.6369×10^{-4}
57	-2.4873	2.1762×10^{-3}	01	0.3868	7.7135×10^{-3}
00	-2.4527	1.1267×10^{-2}	63	-0.3619	3.0409×10^{-2}
31	2.1781	2.3398×10^{-2}	19	-0.3565	1.4991×10^{-2}
72	1.9539	2.0216×10^{-2}	21	-0.3389	3.2438×10^{-2}
88	-1.9151	6.4681×10^{-4}	73	-0.3162	3.2698×10^{-2}
30	-1.5587	2.4409×10^{-2}	02	0.3098	7.6417×10^{-3}
51	1.4762	1.0109×10^{-2}	22	0.3030	2.7601×10^{-2}
50	1.3540	1.0037×10^{-2}	66	0.2748	1.8121×10^{-2}
11	-1.2952	5.0231×10^{-3}	56	-0.2683	2.3946×10^{-3}
87	1.2813	1.2720×10^{-2}	25	0.2247	1.5989×10^{-2}
23	-1.2131	2.6910×10^{-2}	17	-0.2183	3.6273×10^{-2}
74	-1.1767	3.2587×10^{-2}	38	-0.2111	6.6435×10^{-4}
64	1.1428	2.3731×10^{-2}	85	0.1958	4.1448×10^{-4}
60	-1.1346	5.5465×10^{-4}	40	0.1867	6.7666×10^{-4}
13	-1.0363	2.4769×10^{-3}	53	0.1794	1.3984×10^{-2}
35	-1.0152	5.7957×10^{-3}	29	-0.1559	6.2233×10^{-3}
26	-1.0069	3.1832×10^{-2}	39	0.1538	4.4290×10^{-4}
67	0.9278	1.7525×10^{-2}	42	-0.1359	7.2953×10^{-3}
54	-0.9158	2.3805×10^{-3}	20	0.1330	9.2173×10^{-4}
52	-0.9051	2.3491×10^{-3}	41	-0.1272	6.2702×10^{-4}
71	0.8552	1.9949×10^{-2}	82	0.1268	6.4682×10^{-4}
12	0.8358	2.3220×10^{-3}	28	-0.1038	6.6050×10^{-3}
46	0.7259	9.4158×10^{-3}	07	0.1030	6.6437×10^{-4}
65	-0.6920	2.6471×10^{-2}	75	-0.0929	1.7938×10^{-2}
70	0.6651	3.4239×10^{-2}	69	0.0900	2.3117×10^{-2}
15	0.6425	1.1172×10^{-3}	08	-0.0854	1.9408×10^{-3}
47	0.5937	9.4431×10^{-3}	36	0.0847	3.3590×10^{-4}
80	-0.5795	3.4149×10^{-2}	90	0.0836	4.5581×10^{-5}
49	0.5640	6.9340×10^{-3}	43	-0.0797	2.6093×10^{-4}
84	0.5562	7.6356×10^{-4}	14	-0.0766	1.3332×10^{-3}
10	-0.5522	2.8041×10^{-3}	68	-0.0761	1.4963×10^{-2}
76	0.5451	1.8858×10^{-2}	32	-0.0745	2.0748×10^{-3}
62	0.5373	1.3239×10^{-2}	09	0.0496	6.3746×10^{-4}
48	0.5277	7.1636×10^{-3}	37	0.0462	3.7478×10^{-4}
81	0.5218	6.9539×10^{-4}	77	-0.0438	3.0750×10^{-3}
24	0.5206	2.0542×10^{-2}	79	0.0288	3.1391×10^{-3}
27	0.5132	3.3043×10^{-2}	34	-0.0206	1.9660×10^{-3}
04	-0.4836	1.1262×10^{-2}	05	0.0176	9.6553×10^{-3}
44	0.4811	3.2205×10^{-3}	89	0.0165	3.1549×10^{-2}
18	0.4788	1.1043×10^{-2}	16	-0.0136	6.3249×10^{-4}
59	-0.4441	1.2642×10^{-3}	06	0.0112	9.4690×10^{-3}
86	0.4393	6.8539×10^{-4}	45	-0.0090	1.3192×10^{-4}
03	-0.4289	1.1060×10^{-2}			

TABLE S4. Full list of optimized coefficients for $\lambda = 10$ in descending order. The coefficients are calculated as a mean over 10 optimization trials with different initial parameters, and the standard deviations are also calculated from that data.

index	α_i	standard deviation	index	α_i	standard deviation
58	0.8306	3.5528×10^{-11}	81	-0.0426	1.2914×10^{-10}
57	-0.6144	2.7921×10^{-9}	01	-0.0422	6.8381×10^{-11}
12	0.6061	2.3452×10^{-9}	04	-0.0379	3.6555×10^{-10}
55	0.5980	6.3127×10^{-10}	45	-0.0372	2.2530×10^{-9}
11	-0.5796	1.5295×10^{-9}	18	0.0372	3.6965×10^{-9}
53	-0.3841	3.6147×10^{-10}	68	0.0352	3.5254×10^{-9}
88	0.3787	1.0132×10^{-10}	65	-0.0350	1.5159×10^{-10}
30	-0.2475	1.5217×10^{-9}	50	0.0349	1.7245×10^{-10}
56	-0.2391	3.0540×10^{-9}	09	0.0317	1.2569×10^{-9}
61	-0.2257	3.9281×10^{-10}	51	0.0316	1.4641×10^{-10}
87	-0.2200	3.5622×10^{-10}	20	0.0313	3.2898×10^{-9}
15	-0.2189	3.5264×10^{-10}	84	0.0293	1.8027×10^{-10}
31	0.2153	1.7952×10^{-9}	34	0.0292	1.8532×10^{-9}
00	0.2084	1.0023×10^{-7}	64	0.0280	3.1097×10^{-9}
26	0.1699	2.0812×10^{-9}	41	-0.0280	6.1336×10^{-11}
27	-0.1531	1.8384×10^{-9}	83	0.0267	2.9348×10^{-10}
52	-0.1359	8.2253×10^{-11}	02	-0.0258	7.9951×10^{-11}
43	-0.1239	9.3277×10^{-10}	80	-0.0249	9.6400×10^{-10}
76	-0.1054	3.8599×10^{-9}	66	0.0240	2.8176×10^{-9}
75	0.0983	3.9213×10^{-9}	40	0.0238	1.2308×10^{-10}
13	0.0930	3.2933×10^{-9}	05	-0.0232	2.7483×10^{-10}
71	0.0898	3.4497×10^{-9}	89	-0.0231	3.0971×10^{-10}
60	0.0847	5.6629×10^{-10}	33	-0.0227	4.5047×10^{-9}
37	0.0800	2.0658×10^{-10}	10	-0.0213	3.0889×10^{-9}
25	0.0775	3.7010×10^{-9}	17	-0.0197	1.4371×10^{-9}
54	-0.0764	1.8622×10^{-10}	22	-0.0177	1.9466×10^{-9}
70	0.0752	8.2912×10^{-10}	85	-0.0147	2.2215×10^{-10}
69	-0.0711	2.7979×10^{-9}	74	0.0146	4.9195×10^{-11}
19	-0.0684	2.2126×10^{-9}	24	0.0146	2.4496×10^{-9}
23	-0.0677	1.2557×10^{-9}	08	-0.0137	3.4721×10^{-9}
03	0.0676	2.7891×10^{-10}	63	0.0136	4.5148×10^{-10}
39	-0.0646	1.6649×10^{-10}	21	0.0129	1.4208×10^{-9}
07	-0.0615	1.2193×10^{-9}	79	-0.0117	7.3789×10^{-10}
49	-0.0595	2.4875×10^{-10}	29	0.0086	4.0031×10^{-9}
72	-0.0594	3.5546×10^{-9}	32	0.0083	1.9369×10^{-9}
06	0.0588	3.5111×10^{-11}	48	-0.0078	2.5259×10^{-11}
82	-0.0554	5.5851×10^{-10}	14	0.0066	3.6773×10^{-10}
78	0.0527	6.9169×10^{-10}	42	-0.0064	4.6971×10^{-9}
90	0.0504	8.0539×10^{-10}	77	0.0059	1.0523×10^{-9}
86	0.0495	3.2697×10^{-11}	36	0.0057	2.3601×10^{-10}
62	-0.0472	3.4940×10^{-9}	35	0.0035	4.2877×10^{-9}
16	0.0455	8.4477×10^{-10}	28	-0.0035	3.9852×10^{-9}
46	0.0442	1.4667×10^{-11}	59	-0.0026	7.3267×10^{-10}
47	-0.0432	1.8039×10^{-10}	38	0.0022	4.3125×10^{-10}
73	-0.0431	3.1798×10^{-10}	44	-0.0017	4.6810×10^{-9}
67	-0.0430	2.7864×10^{-9}			

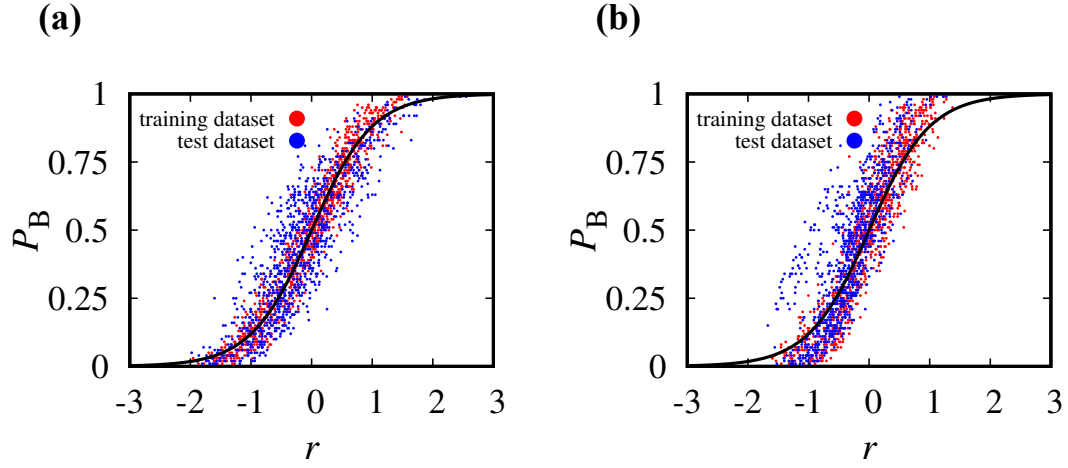


FIG. S2. Committor distributions of the training (red) and test (blue) datasets as functions of the optimized coordinate r for the cases of (a) $\lambda = 0$ and (b) $\lambda = 10$. The sigmoid function $p_B(r) = [1 + \tanh(r)]/2$ is shown in black line.

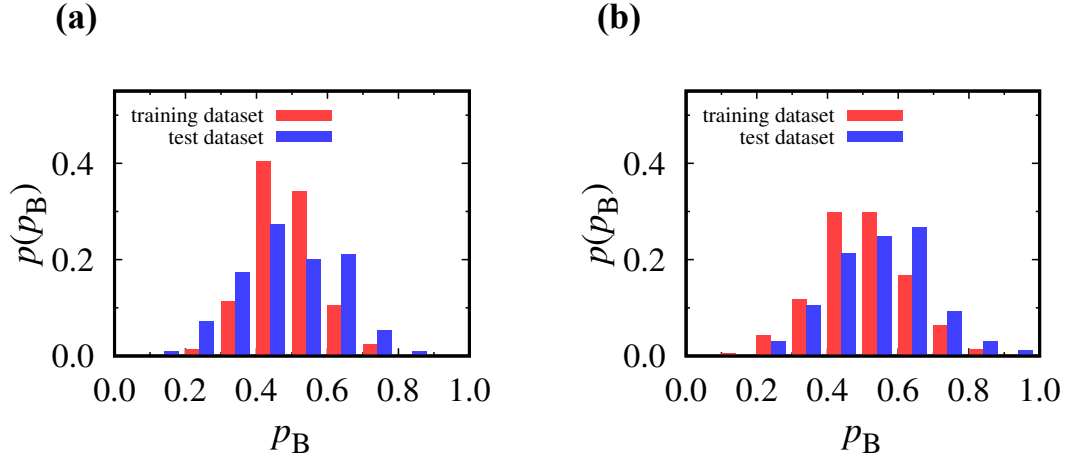


FIG. S3. Probability of p_B at about the transition state of r ($-0.2 \leq r \leq 0.2$) for the cases of (a) $\lambda = 0$ and (b) $\lambda = 10$. Red and blue bars are for training and testing datasets, respectively.